Materials & Design 258 (2025) 114568

Contents lists available at ScienceDirect

Materials & Design

journal homepage: www.elsevier.com/locate/matdes

Insights into the quasi-static mechanics of transversely isotropic polymer foams

Paolo Iaccarino [a,b,c,*], Pietro Sisti [d], Dino Ferri [d,**], Ernesto Di Maio [b,c]

[a] Scuola Superiore Meridionale, Largo San Marcellino 10, Naples, 80138, Italy
[b] Dipartimento di Ingegneria Chimica, dei Materiali e della Produzione Industriale, University of Naples Federico II, P.le Tecchio 80, Naples, 80125, Italy
[c] foamlab, University of Naples Federico II, P.le Tecchio 80, Naples, 80125, Italy
[d] Rheology and Processability Laboratories, Versalis S.p.A., Via G. Taliercio 14, Mantova, 46100, Italy

ARTICLE INFO

Keywords:
Microstructral anisotropy
Polymer foams
Batch foaming
Polystyrene
Polydispersity
Mechanics

ABSTRACT

Owing to their favorable balance of mechanical performance, lightness, and cost-effectiveness, polymer foams are the material of choice in numerous structural applications, where knowledge of the relationship between their microstructure and mechanical behavior is needed for design purposes. This research investigates how *microstructural anisotropy* affects the quasi-static mechanics of transversely isotropic polymer foams. Such foams were designed and produced by expanding polystyrene preforms with different polydispersity indices in cylindrical molds via a batch-foaming method. Microstructural anisotropy was defined to include both the aspect ratio and orientation of the cell, allowing us to apply the well-known homogenized rectangular cell model by Gibson and Ashby (1997) and isolating the effect of microstructural anisotropy. We observed that Young's modulus increased more than threefold and non-linear properties more than twofold within a microstructural anisotropy range from 0.69 to 1.43. Additionally, it is shown that the rheology of the base polystyrene influenced anisotropy development. In conclusion, design maps for transversely isotropic foams are proposed. These findings improve our understanding of the *process-structure-property* relationship in anisotropic polymer foams, fostering a more effective and efficient use of such ubiquitous materials.

1. Introduction

Polymer foams are lightweight materials with process-tunable mechanical properties, widely adopted in various structural applications, such as sports goods [1], automobiles [2], and construction [3]. With the continuous development of new technologies, novel polymer foams are being proposed for these applications, including nanocellular [4,5], composite [6], auxetic [7,8], shape-memory [9], functionally-graded [10] and topologically optimized [11] foams.

The mechanical properties of polymer foams primarily depend on the base polymer (elastomeric, thermoplastic, thermosetting, or even reinforced) from which the foams are made [12–16]. When considering semi-crystalline polymers, the degree of crystallinity has the known effect of improving the stiffness and strength of the base material [17,18], thus enhancing the same properties of the resulting polymer foam [19–22]. Regardless of the selected polymer, the molecular orientation in the cell walls developed during the expansion process can also influence the mechanical properties of the foam [23].

Once the base polymer has been selected [24], the mechanical properties of the foam can, in principle, be related to independent parameters - on various scales [25] - of the foam, which influence these properties to varying degrees [26,27].

The most important independent parameter of polymer foams is density [28]. In fact, a plethora of researchers demonstrates the primary effect of relative density on the mechanical properties of polymer foams, such as Young's modulus [29,14,30–33], peak stress (if applicable) [34,35], collapse stress [36], plateau stress [31,37,38], and total energy absorption [34,37,39]. As a general rule, it can be inferred that the aforementioned properties vary according to a power law with respect to the *relative* density, i.e., the ratio between the density of the foam and the density of the base polymer [28,40].

* Corresponding author at: Scuola Superiore Meridionale, Largo San Marcellino 10, Naples, 80138, Italy.
** Corresponding author at: Rheology and Processability Laboratories, Versalis S.p.A., Via G. Taliercio 14, Mantova, 46100, Italy.
E-mail addresses: paolo.iaccarino-ssm@unina.it (P. Iaccarino), pietro.sisti@versalis.eni.com (P. Sisti), dino.ferri@versalis.eni.com (D. Ferri), edimaio@unina.it (E. Di Maio).

https://doi.org/10.1016/j.matdes.2025.114568
Received 24 June 2025; Received in revised form 3 August 2025; Accepted 11 August 2025

Available online 14 August 2025

Then, all the parameters that determine the mechanical properties of the foam are related to its microstructure [41,26], such as cell size and shape [42–44,23,45–47], the amount of open or closed cells [29], and the geometry of the struts and walls [48,49].

A particularly relevant characteristic of the microstructure is the *microstructural anisotropy*, which is crucial to define the mechanical properties of a polymer foam, as it is responsible for its macroscopic anisotropic mechanical behavior. Microstructural anisotropy has the potential to alter the quantitative and qualitative macroscopic behavior of polymer foams [50]. Compared to density, microstructural anisotropy has been investigated much less extensively [51,52]. For microstructural anisotropy, we do not restrict our focus to the anisotropy (e.g., an aspect ratio different from 1) of the foam cells, but also include their orientation and size distributions, which are crucial for determining the macromechanical behavior of the polymer foam [53].

The effect of microstructural anisotropy is generally investigated by testing the same type of anisotropic foam in different directions [54–57]. It is well known that linear and nonlinear mechanical properties (such as Young's modulus, peak stress, and collapse stress) are higher when the foams are loaded in the direction in which the cells are mainly elongated or oriented, typically the foam rise direction. Moving from the rise direction to the transverse direction, a transition often occurs from a peak in the stress-strain curve to monotonic behavior [58–62,44,63]. In classical homogenized micromechanical models [64], these different behaviors have been attributed to the response of *a single type* anisotropic microstructural elements (for example, prismatic cells with an aspect ratio different from 1) that are repeated periodically in space [65,28]. However, the parameters of such microstructural elements should include statistical information about the homogenized foam microstructure in their definition, which is a nontrivial step. To emphasize the importance of incorporating distributions in microstructural anisotropy, Luan et al. numerically demonstrated that the presence of cell size polydispersity produces a stable monotonic stress-strain response, even when cells are highly anisotropic and oriented parallel to the (uniaxial) load [66]. In addition, Wang et al. demonstrated that polydispersity in the orientation distribution of cells with respect to the loading direction also leads to a stable monotonic response, which is characteristic of a foam that is loaded in the transverse direction [67].

In such a framework, designing and producing mechanically isotropic and anisotropic foams with the same density for accurate characterization is not a simple task: In fact, microstructural anisotropy is often the result of uncontrolled, mostly undesired oriented growth of cells due to process constraints, and not a design variable [58,57]. A few approaches have been proposed to design anisotropic foams for a rigorous study of the effect of microstructural anisotropy. Bao et al. produced mechanically anisotropic polystyrene (PS) foams by using batch foaming to study the effect of such anisotropy on impact strength. In their case, isotropic samples were produced by free expansion (that is, the foam allowed to grow without any mechanical constraint), while anisotropic samples were produced by mechanically constrained oriented growth. They reported that cells oriented perpendicular to the impact direction could significantly improve the impact strength of PS foams [23]. Later, Bernardo et al. proposed a two-step foaming process to produce large anisotropy ratios. They reported that, maintaining a constant density (140 ± 2 kg/m^3), the Young's modulus can increase up to 2.63 times when their measure of microstructural anisotropy spans from 2.95 to 3.75 [68]. However, the absence of the corresponding isotropic foam limits the ability to fully compare macroscopic mechanical properties. In addition, the characterization did not appear to include non-linear mechanical behavior. Sauter et al. investigated the effect of anisotropy on Young's modulus and on the recovery of a shape-memory polymer foam with the same density produced by physical batch foaming. The nonlinear mechanical properties were not investigated, and a non-negligible difference in cell size was also reported (the average diameter of the isotropic foam was ~ 390 μm, while the average diameter of the anisotropic foam was ~ 520 μm) [69]. Oliveira-Salmazo et al. produced different anisotropic natural rubber foams with almost the same relative density (~ 350 kg/m^3) and almost the same cell size (~ 430 μm) via chemical batch foaming and suitably designed preforms, but reported data on Young's modulus only [70].

Important questions remain regarding the relationship between microstructural anisotropy and both the linear and non-linear mechanical properties of anisotropic foams. Consequently, the design of the microstructure - along with the achievement of desired microstructures in polymer foams for specific applications - currently lacks optimization.

Within this framework, the present work focuses on designing and producing transversely isotropic polymer foams and their isotropic counterparts, with the primary aim of understanding how microstructural anisotropy influences the quasi-static, linear, and non-linear mechanical behavior of these ubiquitous materials. To this end, we utilized physical batch foaming combined with specially designed base material preforms to produce three types of foam within the same extremely narrow density range: two exhibiting microstructural anisotropy (both transversely isotropic) and one with an isotropic microstructure. PS was selected as the base polymer since (i) it is widely used in the foaming industry and hence extensively studied in the literature for fundamental research on polymer foam production, and (ii) it is amorphous, allowing us to avoid any effects of crystallinity on the mechanical properties of the resulting foams. To further extend the validity of such an investigation, the foams are produced using three different types of PS, each characterized by a distinct Molecular Weight Distribution (MWD) and a different polydispersity index (PDI). However, all the PSs share the same Melt Flow Index (MFI). Maintaining the same MFI allows us to keep the foaming process conditions as close as possible among the various PSs. The microstructural characteristics of the foams are analyzed using Scanning Electron Microscopy (SEM), and their linear and non-linear mechanical properties are evaluated in quasi-static uniaxial compression. We show that the mechanical behavior of anisotropic foams can be described based on their microstructure by assuming that the microstructural anisotropy - defined here as encompassing all statistical parameters of the microstructure - corresponds to the *aspect ratio* of an equivalent rectangular cell periodically repeated in space, allowing us to recover the classical homogenized model originally proposed by Gibson and Ashby [64]. In doing so, we are then able to isolate the contribution of microstructural anisotropy to the linear and non-linear macroscopic mechanical properties of the foams. Finally, we also demonstrate that the rheology of the base material plays a crucial role in the development of anisotropy during processing, and that the low-molecular-weight tail of the MWD is a key factor in determining the average cell size. These findings are further supported through an additional experimental campaign using lower-density (LD) samples. In conclusion, we propose useful design maps for the mechanical properties of transversely isotropic foams.

2. Materials

Three linear PSs obtained by radical polymerization with different Molecular Weight Distribution (MWD) - characterized by the polydispersity indices (PDI) - are considered, achieved by appropriately selecting the amount of chain transfer during the polymerization process and tuning the temperature profile of the reactors. The MWD was assessed via Gel Permeation Chromatography (GPC), performed at room temperature using a GPC apparatus equipped with an Alliance 2695 injection system, a W2489 UV detector, and a W2414 differential refractive index detector (Waters TA Instruments, Delaware, USA). Separation was achieved on four columns 30 cm × 7.8 mm, with 5 μm particles and nominal pore sizes $10^6, 10^5, 10^4$ and 10^3 Å (Phenogel™ GPC/SEC columns, Phenomenex, California, USA). Tetrahydrofuran served as the mobile phase at 1 ml/min and as the solvent for polymer samples, which were prepared at 2.5 mg/mL. The GPC traces of the PSs are shown in Fig. 1(a). The three PSs used in this study are designated as PS 2.3, PS 2.7, and PS 4.3, with the numbers indicating the PDI.

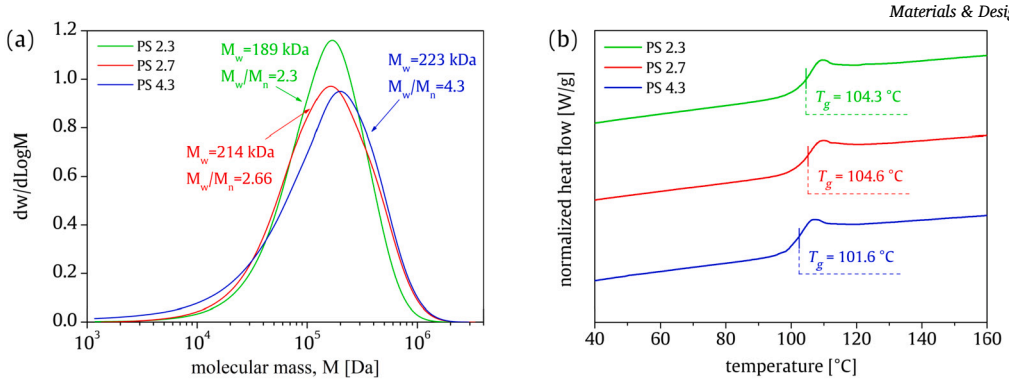

Fig. 1. (a) GPC traces of the different PSs. (b) DSC measurement (exo down) of the different PSs.

The three PSs have the same Melt Flow Index (MFI) in the range of experimental error. We measured the MFI at 200 °C according to ISO 1133 (with a mass of 5 kg) using a melt flow tester (model MF50, Instron, Norwood, MA, USA), obtaining 6.6 – 6.7 g/10 min for PS 2.3, 6.6 – 6.7 g/10 min for PS 2.7, and 6.6 – 6.8 g/10 min for PS 4.3.

The glass transition temperature (T_g) is measured using a Differential Scanning Calorimeter (DSC 2500, TA Instruments, Delaware, USA), with a scanning rate of 20 °C/min, and it is assumed that T_g corresponds to the midpoint temperature of the step change in the thermal curve, following the procedure described in ASTM D746 - 08 [71]. The DSC traces are presented in Fig. 1(b). As observed, PS 4.3 clearly exhibits a pronounced low molecular weight tail that in turn lowers the glass transition temperature of ~ 3 °C compared to PS 2.3 and PS 2.7.

For foaming experiments, we used CO_2 (purity 99.99%) as a blowing agent, supplied by SOL S.p.A. (Monza, Italy).

3. Sample production

The production process of the foamed samples consists of two consecutive steps: (1) preform production and (2) gas foaming. In step (1), we begin with PS granules to produce cylindrical PS preforms. In step (2), we expand these preforms in a mold using CO_2.

3.1. Preform production

The aim of the present step is to produce cylindrical PS preforms with three different aspect ratios, h_0/d_0 (where h_0 is the height and d_0 is the diameter), while maintaining a constant mass starting from PS granules. In this way, following the gas foaming step in the same mold, we can obtain foamed PS samples with the same density but with differing anisotropy.

Preventing the molecular orientation of macromolecules and eliminating any trace of preexisting granules in the preform is of paramount importance, as these factors can result in microstructural defects after the gas foaming step. This will strongly impact the mechanical properties of the foam and lead to a significant dispersion of the results (see Figure SI 1 of *Supporting Information* for further details). For this reason, two high-temperature stages are conducted to produce the plates from which the cylindrical PS preforms are then cut: (i) the granules are first heated to 200 °C and molded into plates of dimensions (60×60×4) mm^3 using an injection molding machine (Engel ES-50, ENGEL AUSTRIA GmbH, Schwertberg, Austria); (ii) these plates are then re-heated to 180 °C and subsequently reshaped into plates of dimensions (70×70×2) mm^3, (50×50×3) mm^3 and (60×60×4) mm^3 using a compression molding press (Hydraulic Unit 3912, CARVER, Indiana, USA). After stage (i), the memory of the preexisting granules is completely erased, whereas after stage (ii) the molecular orientation is fully relaxed.

The cylindrical PS preforms are machined from the plates using an automatic cutting machine (CNC Pantograph, GPprotoCNC, Bologna, Italy). Three types of cylindrical PS preforms, each with the same mass of 151 ± 7 mg are obtained to ensure that the densities of the resulting PS foam after expansion are as consistent as possible. Each of the three types of preforms shows a different aspect ratio:

- $h_0/d_0 = 0.21$ ($h_0 = 2$ mm, $d_0 = 9.5$ mm);
- $h_0/d_0 = 0.36$ ($h_0 = 3$ mm, $d_0 = 8.3$ mm), equal to the mold aspect ratio (see subsection 3.2);
- $h_0/d_0 = 0.58$ ($h_0 = 4$ mm, $d_0 = 6.9$ mm).

3.2. Gas foaming

The gas foaming step is performed in a 0.3 L thermoregulated pressure vessel (model BC-1, High Pressure Equipment Co., Erie, PA, USA) introduced in the work of Marrazzo et al. [72] and properly modified (schematic in Fig. 2(a)). The electrical heater of the pressure vessel is controlled by a PID thermoregulator (mod. 1850, Gefran S.p.A., Provaglio d'Iseo, Brescia, Italy), which controls the temperature of the heating jacket using a J thermocouple. The sample temperature is measured using a Pt100. A pressure transducer (TK, Gefran S.p.A., Provaglio d'Iseo, Brescia, Italy) is used to measure pressure during the saturation step. The pressure discharge system consists of a discharge ball valve (model 15-71 NFB, High Pressure Equipment Co., Erie, PA, USA) and an electromechanical actuator (model 15-72 NFB TSR 8, High Pressure Equipment Co., Erie, PA, USA). The Pressure Drop Rate (*PDR*) is measured through a PLC (SIMATIC S7-1200 CPU, Siemens, Munich, Germany) with a sampling rate τ_m = 1 ms, following the procedure proposed by Miele et al. [73]. The pressure vessel is connected to a vacuum pump (LABOPORT N 840, KNF Neuberger SAS, Village-Neuf, France) and to the gas cylinder through two ball valves (Multipurpose Ball Valve SK Series 8, Swagelok Company, Ohio, USA).

To obtain properly shaped foam samples, each PS preform is placed in a cylindrical mold with a height of $H = 8.4$ mm and a diameter of $D = 23.1$ mm (Fig. 2(b)). The PS foams are produced according to the following procedure: the mold is inserted into the pressure vessel described above and heated under vacuum conditions until a temperature of $T_i = 100$ °C is reached. The pressure of CO_2 increases to a saturation pressure of P_s (in 1 minute) and the system temperature is brought to a saturation temperature of T_s (in 10 minutes). P_s is maintained constant for a given saturation time of t_s. The pressure is then released at a maximum rate of *PDR* of 50 MPa/s (consistent across all tests) and the foamed sample is produced and shaped by the available mold volume, resulting in a final height of H and a diameter of D.

Given the PS-CO_2 mutual diffusivity coefficient of 3×10^{-10} m^2/s [74,75], t_s is selected as 3600 s for $h_0 = 2$ mm, 5400 s for $h_0 = 3$ mm and 7200 s for $h_0 = 4$ mm. The foaming process is represented schematically in Fig. 2(c).

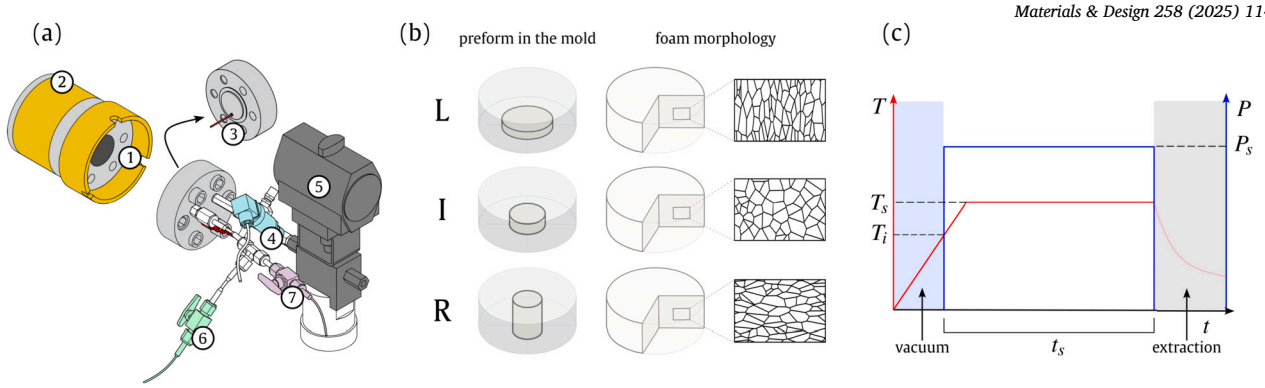

Fig. 2. Schematic of the foaming apparatus: ① pressure vessel; ② heating jacket; ③ Pt100; ④ pressure transducer; ⑤ pressure discharge system; ⑥ to the vacuum pump; ⑦ to the gas cylinder. (b) Schematic of produced foams. The three types of preforms (L, I and R) are expanded the same cylindrical mold: depending on the preform, the expansion can be isotropic (I) or anisotropic (L and R), leading to different morphologies and distribution orientations of the cells in the resulting foam. (c) Schematic of the foaming process.

Table 1
Names, preform names, properties and process parameters of the produced PS foams.

foam name	preform name	PDI [-]	R_{N_0} [-]	ρ [kg/m^3]	SD$_\rho$ [kg/m^3]	T_s [°C]	P_s [bar]	t_s [min]
L-2.3	**pL-2.3**	2.3	0.6	39.8	0.5	114.3	145	60
I-2.3	**pI-2.3**	2.3	1.0	38.8	1.3	114.3	145	90
R-2.3	**pR-2.3**	2.3	1.6	41.1	1.0	114.3	150	120
L-2.7	**pL-2.7**	2.7	0.6	41.2	0.8	114.3	145	60
I-2.7	**pI-2.7**	2.7	1.0	39.6	0.7	114.3	145	90
R-2.7	**pR-2.7**	2.7	1.6	39.6	0.7	114.3	150	120
L-4.3	**pL-4.3**	4.3	0.6	38.0	1.6	113.8	145	60
I-4.3	**pI-4.3**	4.3	1.0	37.3	0.9	113.8	145	90
R-4.3	**pR-4.3**	4.3	1.6	37.4	0.6	113.8	150	120

3.3. Adopted nomenclature

Let us now define the *nominal theoretical anisotropy*, R_{N_0}, as the ratio between the aspect ratio of the preform and the aspect ratio of the mold, H/D:

$$R_{N_0} = \left(\frac{h_0}{d_0}\right)\left(\frac{H}{D}\right)^{-1} . \quad (1)$$

It is intuitive to expect that when $R_{N_0} = 1$, at the pressure release, the flow front of the expanding preform will be free until it is constrained *at the same time* in the longitudinal direction by the upper base wall of the mold and in the radial direction by the lateral wall of the mold, resulting in an isotropic foam. In contrast, if $R_{N_0} < 1$ (> 1), it is expected that the flow front of the expanding preform will first encounter the lateral wall of the mold (upper base wall) and only later the upper base wall of the mold (lateral wall), resulting in a mechanically anisotropic foam, with cells preferentially elongated and/or oriented in the longitudinal (radial) direction. A visualization of the mentioned process is reported in Media 1 of *Supporting Information*. In the present work, we refer to the longitudinal direction as direction L and to the radial direction as direction R, and hence the nomenclature of the PS foam samples is assigned accordingly.

The sample name, the PDI, R_{N_0}, the average density ρ and standard deviation (SD) of five or more samples of the same type (measured as described in the Methods), together with the set of process parameters (T_s, P_s, t_s) for each type of foam sample are reported in Table 1. The data for each PS foam sample required to calculate the values in Table 1 are presented in Table SI 1 of the *Supporting Information*.

4. Sagging experiments

For *sagging experiments*, we refer to experiments in which we aim to measure the change in the aspect ratio of the preform during CO_2 solubilization. In fact, it is well known that many polymers - including PS - are highly plasticized under high-pressure of CO_2, often resulting in a considerable decrease in glass transition temperature [76–79], and a decrease in zero-shear viscosity [80]. During the solubilization time (that is, when the PS is plasticized with CO_2) of the gas foaming process, if the zero-shear viscosity is sufficiently low, the preform can flow under its own weight, potentially leading to a significant deviation of its aspect ratio from R_{N_0}. This will directly influence the aspect ratio and distribution of the cells, thus directly affecting the resulting mechanical properties. Therefore, we can define the *time-dependent theoretical anisotropy*, $R_N(t)$, as follows:

$$R_N(t) = \left[\frac{h(t)}{d(t)}\right]\left(\frac{H}{D}\right)^{-1} \quad \text{with } t \in [0, t_s] , \quad (2)$$

where $h(t)$ and $d(t)$ are the actual diameter and height of the preform during solubilization, respectively. It is evident that $h(t=0) = h_0$ and $d(t=0) = d_0$ and hence $R_N(t=0) = R_{N_0}$.

In this framework, the aim of the sagging experiments is to observe the evolution of $R_N(t)$ until the saturation time is reached. Obviously, as the aime of the work is to analyze the effect of anisotropy on mechanical properties, it is of paramount importance to precisely define the same.

Sagging experiments are performed in the *mini-batch* apparatus configured in the view cell arrangement, first introduced by Tammaro et al. [81]. The mini-batch is a miniaturized pressure vessel equipped with two heating plates and four ports: through the first port, a Pt100 temperature sensor (positioned as close as possible to the sample) is installed to enable sample temperature measurement; the second port is connected to the gas cylinder (or to the vacuum pump when necessary); the third port is connected through a "T" fitting to both a pressure transducer (mod. 1850, Gefran S.p.A., Provaglio d'Iseo, Brescia, Italy) and a ball valve (10–80 NFH ball valve, High Pressure Equipment Company, Erie, USA), which is activated by an electromechanical actuator and allows for the release of CO_2; the fourth port, the view port—which is also used for the introduction of the sample—is closed with a 1/2" NPT sapphire window (Precision Sapphire Technologies Ltd., Vilnius, Lithuania)

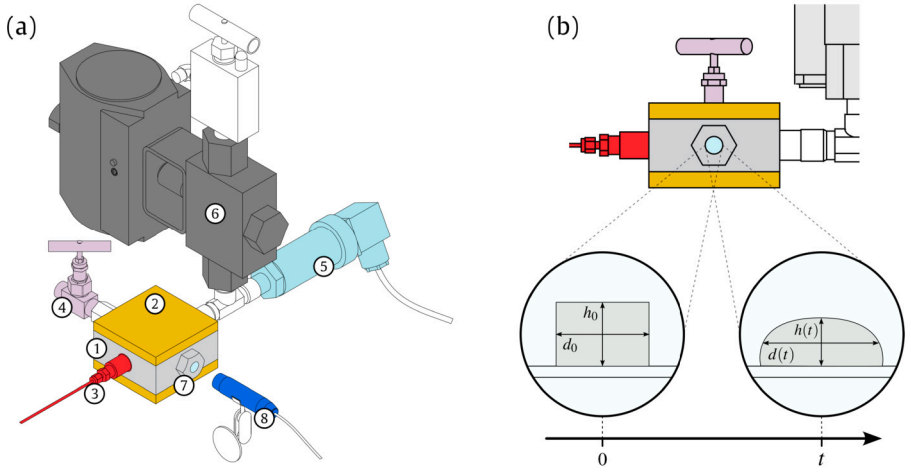

Fig. 3. (a) Schematic of the mini-batch apparatus in the view cell configuration: ① pressure vessel; ② heating plate; ③ Pt100; ④ to the gas cylinder (or to the vacuum pump); ⑤ pressure transducer; ⑥ pressure discharge system; ⑦ sapphire window; ⑧ digital microscope. (b) Schematic of the sagging measurement.

to permit visual observation and video recording of the experiments through a digital microscope (Microscope USB PCE-MM 800, PCE Instruments, Soultz-sous-Forêts, France). The mini-batch in the view cell configuration is schematized in Fig. 3(a).

For each type of preform, the related foaming procedure is reproduced, as illustrated in Fig. 2(c), and the video recording of the evolution of the preform shape (through the view cell) starts when the pressurization begins ($t = 0$) and ends at t_s. An image is saved automatically every 30 seconds, resulting in a video (see Media 2, for example). Then $d(t)$ and $h(t)$ are obtained *a posteriori* by image analysis of the preform (using Fiji software [82]) and $R_N(t)$ can be properly calculated. The schematic of the measurement is reported in Fig. 3(b). We provide an estimate of the error in the measurement of $R_N(t)$ for each preform as follows. We assume that (i) the volume does not change during measurement and (ii) the shape of the preform remains cylindrical (the most significant assumption); hence, we can compute $d(t)$ from the experimental measurement of $h(t)$ and vice versa. In this manner, two new measurements of $R_N(t)$ are obtained, which are considered reasonable bounds for the true $R_N(t)$.

5. Methods

5.1. Density measurement

To measure the density of the PS foams produced (ρ), we apply the buoyancy method along with the following equation:

$$\rho = \frac{m_a}{m_a - m_w}(\rho_w - \rho_a) + \rho_a \ , \tag{3}$$

where m_a is the weight of the sample in air, m_w is the weight of the foam in water, ρ_a is the density of air and ρ_w is the density of water. At room temperature ($23 \pm 2\,^\circ$C), $\rho_a = 0.00120 \pm 0.00002$ g/cm^3 and $\rho_w = 0.9975 \pm 0.0005$ g/cm^3 [83]. The values m_a (± 0.0005 g) and m_w (± 0.0005 g) are measured using an analytical balance (MS Semi-Micro Model, Mettler Toledo, Milan, Italy). The measurement error in the density of the foams (computed as shown in Appendix A) is approximately 0.2 kg/m^3, which we consider negligible for the scope of the present work since it is one order of magnitude less than the standard deviation obtained for a set of ideal iso-density samples (see Table 1).

5.2. Microscopy

A Scanning Electron Microscope (TESCAN MIRA II, Tescan Group, Brno, Czech Republic) is used to analyze the cellular structure of the foams. Foams are cut into sections and then coated with a thin layer of gold/palladium alloy ($\sim 1 - 10$ nm) prior to image acquisition using the sputter coating technique (Q150T ES Plus, Quorum Technologies, Lewes, UK). To obtain a mechanically meaningful indication of the anisotropy of the foam, we first define the *microstructural anisotropy*, R, as:

$$R = \frac{C_l}{C_r} \ , \tag{4}$$

where C_l is the mean chord in the longitudinal direction, and C_r is the mean chord in the radial direction. To compute C_l and C_r, we draw inspiration from the Intersecting Line Method (ILM) of ASTM D 3756-15 [84] and propose the following procedure. We superimpose a 4×4 grid on the SEM images, where the grid lines are oriented in the longitudinal and radial directions. Then, we identify all the intersections between the grid and the cell edges, and we automatically compute the chords, which are the distances between subsequent (i.e., on the same grid line) intersections. From the distributions of the chords in both directions, we can obtain their means C_l and C_r. The uncertainty in the measurement of R is determined as reported in subsection A.2. It is easy to see that if $R = 1$, the cells are mainly spherical or, if not, they will be randomly oriented in space, and the macroscopic mechanical behavior is expected to be isotropic. If $R > 1$, cells will be elongated and oriented primarily in the longitudinal direction, while if $R < 1$, cells will be elongated and oriented primarily in the radial direction: in both cases, macroscopic mechanical behavior is expected to be anisotropic. Hence, we can consider R as a homogenized parameter of the microstructure under the (experimentally verified) assumption that the material is statistically uniform, allowing for the derivation of homogenized properties (such as the Young's modulus and stresses of the foam). Two foams per type are imaged and therefore two independent measurements of R are obtained. Then we compute the average between the two measurements and its uncertainty, δ_R (as reported in subsection A.2).

We can thus estimate the Mean Cell Size (MCS) value as follows:

$$\mathrm{MCS} = \left(\frac{4}{\pi}\right)^2 \frac{N_l C_l + N_r C_r}{N_l + N_r} \ . \tag{5}$$

For additional details on the derivation of the factor $(\pi/4)^2$ in eq. (5) and its uncertainty, the reader is referred to subsection A.3.

5.3. Uniaxial compression testing

A universal testing machine (Model 5966, Instron, Norwood, MA, USA) equipped with a load cell of 10 kN is used to perform uniaxial compression tests. The tests are carried out in a displacement control mode with a strain rate of 0.1 min^{-1} and at room temperature ($25 \pm 2\,^\circ$C). The load cell has been certified as class 0.5 (ISO 7500-1), while the

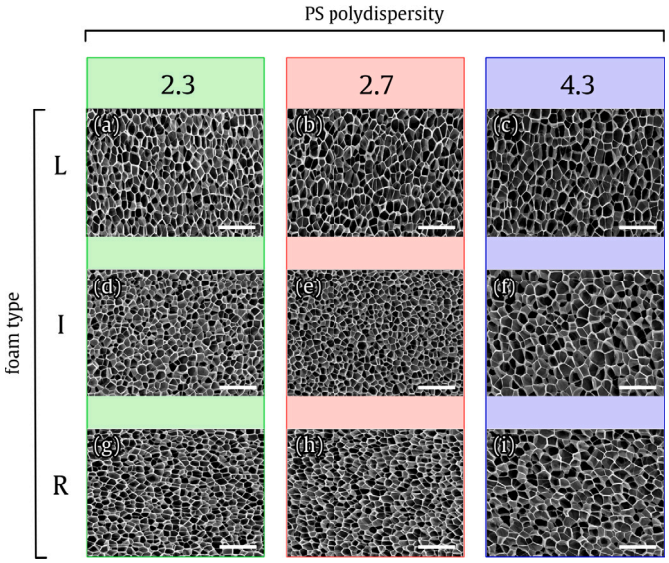

Fig. 4. SEM images of the produced foams. The scale (white segment) corresponds to 200 μm. Row-wise, the longitudinal anisotropic (L), isotropic (I), and radial anisotropic (R) morphologies. Column-wise, the PS polydispersity.

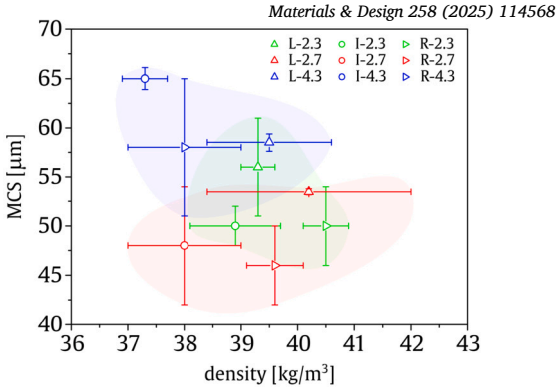

Fig. 5. MCS of the foams as a function of the density. Shaded areas are a visual guide for the range of MCS of the different PSs.

displacement measurement system has been certified as class 0.5 (ISO 9513).

5.4. Rheological measurements

Rotational steady-state measurements were performed in shear using a rotational rheometer (ARES LSII, TA Instruments, Delaware, USA). The samples were compression molded at 190 °C (Hydraulic Unit 3912, CARVER, Indiana, USA) and recovered as disks to fit the rheometer tools. The steady-state viscosity was measured with a cone and plate geometry (cone angle of 0.1 rad) and shear rates ranging from 10^{-3} s^{-1} to 5 s^{-1}. All tests were conducted under a N_2 atmosphere. The temperature was stable within 0.2 °C over the range used in this study. Capillary measurements were performed using a capillary rheometer (RG 20, Göttfert, Buchen, Germany). The viscosity was measured in the shear rate range from 1 s^{-1} to 10^3 s^{-1} and corrected for non-Newtonian effects (i.e., the Rabinowitsch correction). The entry effects (i.e., the Bagley correction) were negligible, considering the length-to-diameter ratio (30) of the capillary and the entry angle (180°) adopted for this work.

6. Results and discussion

6.1. Foams microstructures

The SEM images of the foams produced are presented in Fig. 4(a)-(i). From Fig. 4(c), (f) and (i), it can be observed that PS 4.3 has a larger cell size compared to PS 2.3 and PS 2.7, which both exhibit smaller and comparable cell sizes. This observation is further confirmed by Fig. 5, which presents the MCS of the foams produced as a function of density. When the pressure and the *PDR* are held constant during the foaming process, the cell structure is primarily influenced by the foaming temperature: as the foaming temperature increases, the cell size typically increases [85]. However, in our case, the foams of PS 4.3 - produced at lower temperature - exhibit larger cell size. We therefore believe that, in this specific case, the temperature change has a minor effect and that the base polymer plays a more significant role in the evolution of the foam microstructure.

In fact, an alternative explanation for the different cell sizes could be attributed to the difference in the very low molecular weight tail of the MWD of the PSs. In particular, Stafford et al. highlighted this phenomenon for commercial PS samples foamed with supercritical CO_2, proposing a correlation between the low molecular weight tail and cell size [86]: in more detail, the results of these authors show an increase in cell size with increasing PDI, and that the presence of a molecular component equal to 270 Da was ascribed to be responsible for the increase in cell size. To further investigate this aspect and verify whether the data in the present work agree with such experimental evidence, further investigations are performed by measuring the MWD curve three times, paying close attention to the stability of the baseline. The results are then averaged and used to quantify in the cumulative MWD both the percentage by weight of polymer chains having a molecular weight lower than that between entanglements (M_e = 18000 Da) and the percentage by weight of polymer chains having a molecular weight lower than 2000 Da. To further complete the information, we decide to analyze styrene dimers (S2) and trimers (S3) using the following procedure: we dissolve the different PSs in ethanol and precipitate them in chloroform, and then we used gas chromatography (Trace™1300, Thermo Fisher Scientific, Waltham, MA, USA).

Table 2
Low molecular weight tails and dimers (S2) and trimers (S3) content of the different PSs.

sample	weight < 18000 [%]	weight% < 2000 [%]	S2 [ppm]	S3 [ppm]
PS 2.3	2.9	0.1	377	6928
PS 2.7	2.7	0.1	232	6404
PS 4.3	6.2	0.45	1410	10470

The results are shown in Table 2. It is clearly evident that PS 4.3 exhibits a significant tail of low molecular weights that could justify the fact that in this work we obtain similar results to those of Stafford et al. [86]. Moreover, from Table 2 it is further pointed out that the contribution of dimers and trimers is definitively higher for the PS 4.3 sample. On the one hand, it is interesting to note that the amount of dimers and trimers, as well as the cell size, is not a monotonic function of polydispersity. However, the cell size monotonically increases with the number of dimers and trimers measured, a result that is in excellent agreement with that of Stafford et al. [86]. This aspect has not yet been sufficiently studied in the literature and certainly deserves further investigation.

It is also important to note that the microstructural anisotropy is not exactly the same for all foams produced from the same preforms (i.e., with the same R_{N_0}), particularly for foams of type I and R, as indicated by the values of R of Table 3.

6.2. Quasi-static mechanics

In Fig. 6(a)-(i) we present the results of the uniaxial compression tests. As shown in the schematic of the foams produced in Fig. 2(b), it is essential to emphasize that these tests are carried out in the L direction.

Fig. 6(a)–(c) show representative stress–strain curves for all investigated foams. The shaded bands indicate the range between the minimum

Table 3
Microstructural anisotropy and its uncertainty for each type of foam.

parameter	L-2.3	I-2.3	R-2.3	L-2.7	I-2.7	R-2.7	L-4.3	I-4.3	R-4.3
R [-]	1.43	1.01	0.72	1.45	0.89	0.69	1.45	1.12	0.78
δ_R [-]	0.08	0.02	0.05	0.06	0.02	0.015	0.05	0.06	0.05

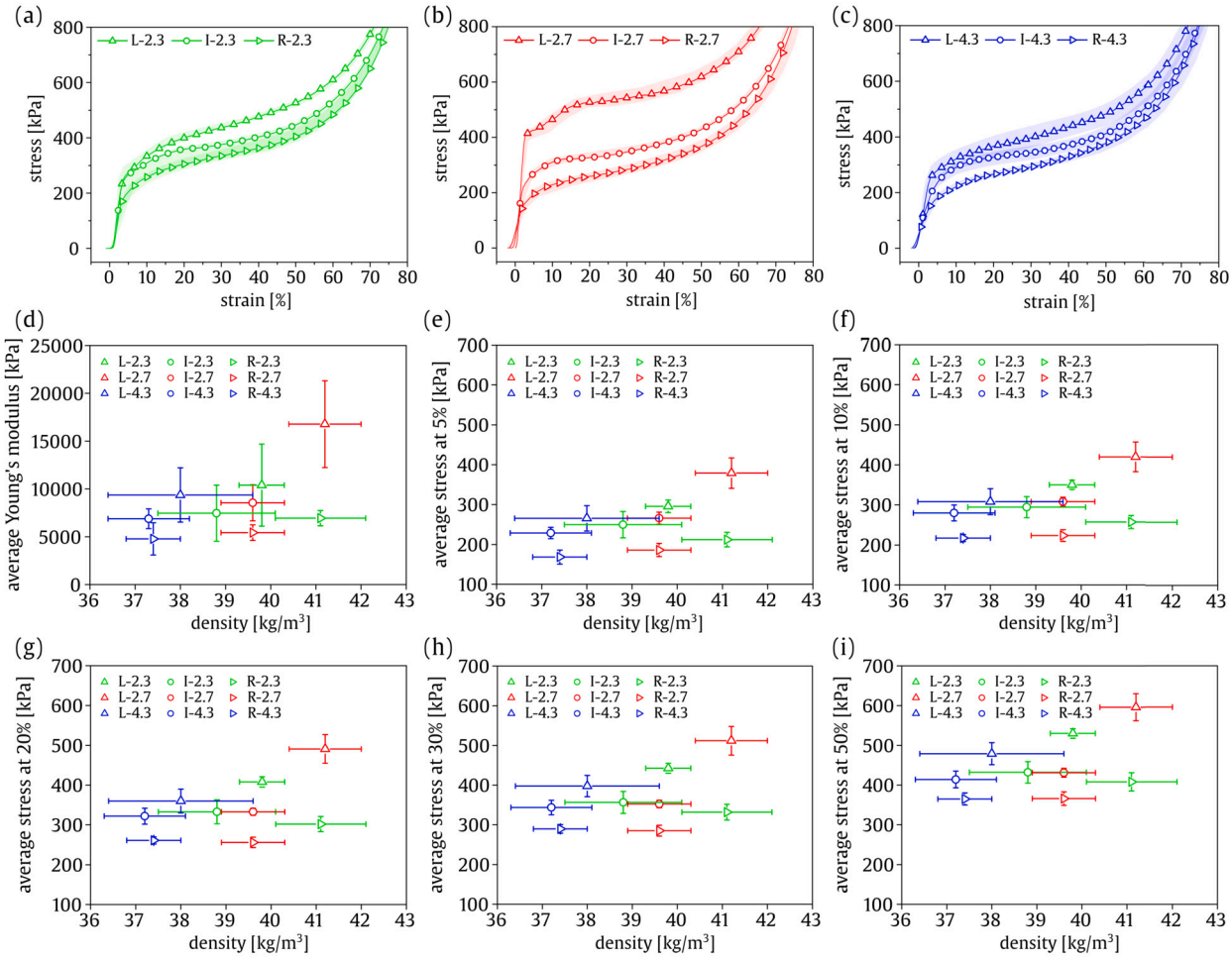

Fig. 6. Results of the uniaxial mechanical tests. (a), (b), and (c) show representative stress-strain curves along with range bands indicating the full range (minimum to maximum) of stress values at each strain level for samples with polydispersity index of 2.3 (green), 2.7 (red), and 4.3 (blue), respectively. From (d) to (i), comparative figures which include all sample types are shown: specifically, figure (d) shows the average Young's modulus versus the average density (standard deviations are included), while figures (e), (f), (g), (h), and (i) show the average stress at 5%, 10%, 20%, 30%, and 50% strain, respectively, plotted against the average density (standard deviations are included).

and maximum values obtained experimentally. It can be observed that foams with cells oriented in the longitudinal direction, which is also the loading direction, exhibit properties that can be up to 150% greater than those of foams with cells oriented in the radial direction (i.e., with cells oriented perpendicular to the loading direction), such as in the case of foams produced by PS 2.7. Upon reaching densification at strain ~ 70%, the curves become closer and almost superimpose, since the density is nearly the same, due to the fact that the densification strain depends mainly on the density and weakly on the microstructural anisotropy [67]. Fig. 6(d)-(i) show the linear (Young's moduli) and non-linear mechanical properties as a function of the density (all data are also reported in *Supporting Information*). Given the very narrow density interval (39.2 ± 2.1 kg/m^3, where here 2.1 kg/m^3 is the half-spread), the effect of microstructural anisotropy becomes particularly evident: all R foams consistently exhibit lower performance than I foams, which in turn fall below L foams, regardless of the base PS. Furthermore, this difference remains essentially unchanged even at increasing stress levels, indicating that microstructural anisotropy has a strong and persistent influence on the mechanical behavior of foams, at least up to 50% strain.

6.3. *Effect of the microstructural anisotropy*

From Fig. 6(a)-(i), it is evident that microstructural anisotropy can significantly affect the mechanical properties of PS foams. However, from an engineering perspective, it is highly beneficial to visualize the effect of the *sole anisotropy* at *exactly the same density*, allowing the mechanical properties to be expressed as a function of the microstructural anisotropy of the foams. To achieve this, we must assume a rescaling law for the mechanical data in relation to density and microstructural anisotropy, allowing us to decouple their relative contributions.

Rescaling procedure. Rearranging the equations of the homogenized rectangular closed cell model by Gibson and Ashby [64], Andersons et al. [87] obtained the result that the modulus in the rise direction for a closed-cell foam can be predicted as:

$$E = E_s \left[\left(\frac{3\phi\gamma}{r+2} \right)^2 r^3 + (1-\gamma)\phi \frac{3r}{2r+1} \right] , \tag{6}$$

where $\phi = \rho/\rho_s$ is the relative density of the foam, γ is the fraction of the material in the cell struts and r is the *aspect ratio of the rectangular periodic cell*, defined as the ratio between its height and its length. Similarly, the foam yield strength, σ_y, can be obtained as [87]:

$$\sigma_y = \sigma_{ys} \left[0.3 \left(\frac{3r\gamma\phi}{r+2} \right)^{3/2} + 0.4(1-\gamma)\phi \frac{3r}{2r+1} \right] , \tag{7}$$

where σ_{ys} is the yield stress of the base material.

We emphasize that this model is based on the homogenization approach. In the homogenization approach, a disordered complex microstructure can be approximated by an idealized geometry periodically repeated in space (in this case, the rectangular closed cell [64]). This approximation facilitates the derivation of effective (or homogenized) material properties, under the assumption that the microstructure is (i) statistically uniform and (ii) the macroscopic fields vary slowly. We assume that (i) and (ii) are valid, which is in fact a common assumption for polymer foams. However, since it is well known that a true foamed microstructure possesses a complicated distribution of orientations and aspect ratios of cells (as illustrated in Fig. 4(a)-(i)), recovering the homogenized parameters of a rectangular periodic closed cell is not straightforward.

To achieve this, we replace r with R in eq. (6) and eq. (7), which represents a homogenized parameter (homogenized based on cell aspect ratio, orientation, etc.) that effectively describes the anisotropy of the foam microstructure. Consequently, we conceptualize microstructural anisotropy as the aspect ratio of the equivalent rectangular periodic closed cell originally proposed by Gibson and Ashby [64].

Hence, for the elastic modulus, we obtain:

$$\hat{E} = E_s \left[\left(\frac{3\phi\gamma}{R+2} \right)^2 R^3 + (1-\gamma)\phi \frac{3R}{2R+1} \right] . \tag{8}$$

For the yield strength of the foam, we obtain:

$$\hat{\sigma}_y = \sigma_{ys} \left[0.3 \left(\frac{3R\gamma\phi}{R+2} \right)^{3/2} + 0.4(1-\gamma)\phi \frac{3R}{2R+1} \right] . \tag{9}$$

In both eq. (8) and eq. (9), we have the explicit dependence on (relative) density and microstructural anisotropy; therefore, we can utilize these equations to rescale the mechanical data.

To rescale all the moduli to the same density, we apply the following procedure. First, a parametric fitting is performed using a nonlinear surface regression approach, where eq. (8) was regressed against the average experimental moduli of Fig. 6(d) (including uncertainty, SD_E, which are also all reported in *Supporting Information*). In this regression, the adjustable parameter is γ, the two independent variables are the relative density (obtained by dividing the average density values of Table 1 by $\rho_s = 1050$ kg/m^3) and R (from Table 3), and we set $E_s = 3000$ MPa. Consequently, the regression problem can be formulated as follows:

$$\hat{\gamma}_E = \arg\min_{\gamma} \sum_{i=1}^{9} \frac{1}{SD_{E_i}^2} \left[E(\phi_i, R_i) - \hat{E}\left(\phi_i, R_i; \gamma\right) \right]^2 . \tag{10}$$

We also emphasize that $i \in [1,9]$ identifies the type and PDI of the foam. Once we have obtained $\hat{\gamma}_E$, we define the density-rescaling coefficient for the $i-th$ modulus, $c_i^E(\phi^*, \phi_i, R_i)$, as:

$$c_i^E(\phi^*, \phi_i, R_i) = \frac{\hat{E}\left(\phi^*, R_i; \hat{\gamma}_E\right)}{\hat{E}\left(\phi_i, R_i; \hat{\gamma}_E\right)} , \tag{11}$$

where ϕ^* is the target density for rescaling. We can obtain the density-rescaled modulus, $E^*(\phi^*, R_i)$, as:

$$E^*(\phi^*, R_i) = c_i^E(\phi^*, \phi_i, R_i) E(\phi_i, R_i) . \tag{12}$$

This rescaling is also applied to the error of the modulus by using the same coefficient.

To rescale all stress data at the same density ϕ^*, we apply a similar procedure. Again, parametric fitting is performed using a non-linear surface regression approach, where eq. (9) was regressed against the average experimental stress data at 10% of Fig. 6 (f) (including uncertainty $SD_{\sigma_{10\%}}$, which are also all reported in *Supporting Information*). In this regression, the adjustable parameter is γ, the two independent variables are the relative density (obtained by dividing the average density values from Table 1 by $\rho_s = 1050$ kg/m^3) and R (from Table 3), and we set $\sigma_{ys} = 60$ MPa [88] (a reasonable value of the flexural strength for PS). Hence, the regression problem can be written as follows:

$$\hat{\gamma}_\sigma = \arg\min_{\gamma} \sum_{i=1}^{9} \frac{1}{SD_{\sigma_{10\%}\,i}^2} \left[\sigma_{10\%}(\phi_i, R_i) - \hat{\sigma}_y\left(\phi_i, R_i; \gamma\right) \right]^2 . \tag{13}$$

Once we have obtained $\hat{\gamma}_\sigma$, we define the density-rescaling coefficients for the stress $c_i^\sigma(\phi^*, \phi_i, R_i)$, as:

$$c_i^\sigma(\phi^*, \phi_i, R_i) = \frac{\hat{\sigma}_y\left(\phi^*, R_i; \hat{\gamma}_\sigma\right)}{\hat{\sigma}_y\left(\phi_i, R_i; \hat{\gamma}_\sigma\right)} . \tag{14}$$

Now, we assume that the density-rescaling coefficients do not change with the stress level, and therefore we can obtain the density-rescaling stress data at X%, $\sigma^*_{X\%_i}(\phi^*, R_i)$, as:

$$\sigma^*_{X\%}(\phi^*, R_i) = c_i^\sigma(\phi^*, \phi_i, R_i)\sigma_{X\%}(\phi_i, R_i) , \tag{15}$$

and such a rescaling is also applied to the error by using the same coefficient.

Rescaled data: the effect of *sole* microstructural anisotropy. In Fig. 7(a)-(f), we report the moduli and stresses rescaled at $\rho = 39.2$ kg/m^3 as a function of R (in subsection A.4 we also report the values of $\hat{\gamma}_E$, $\hat{\gamma}_\sigma$, c_i^E and c_i^σ). It is important to note that since the density interval is already narrow, we obtain $c_i^E, c_i^\sigma \in [0.939, 1.079]$, which means a shift (up or down) of the mechanical data always lower than 8% (the same for the corresponding error). Moreover, the choice of the parameters E_s and σ_{ys} in a reasonable physical interval influences c_i^E and c_i^σ less than 2%.

In Fig. 7(a) we report the rescaled average Young's moduli versus R, and it is possible to note that, in the case of foams from PS 2.7, the average Young's modulus increases from 5360 kPa to 15400 kPa moving from $R = 0.69$ to $R = 1.45$. Foams made from PS 2.3 and 4.3 also show a considerable increase in the average Young's modulus in a similar range of R: from 6520 kPa to 10200 kPa for PS 2.3 and from 5100 kPa to 9900 for PS 4.3. It can be seen that eq. (8) well describes the measured average Young's moduli and hence can be used as a predictive tool (when γ is measured independently) at least in the investigated range of microstructural anisotropy values. It also means that using R as homogenized aspect ratio for the model proposed by Gibson and Ashby [64] is a fair assumption. Furthermore, the linear mechanical behavior of the foams within the investigated range of R appears to depend on the type of foam: foams made from PS 2.7 exhibit a higher Young's modulus than those made from PS 2.3, which in turn demonstrate a higher Young's modulus compared to foams made from PS 4.3. This effect cannot be attributed to the Young's modulus of the base PSs, as it has been shown to be independent of M_n and M_w (in our investigation ranges) [89].

In Fig. 7(b)-(f) we report the rescaled average stresses at 5%, 10%, 20%, 30% and 50% of strain versus microstructural anisotropy. In particular, in Fig. 7(c), we also report the fitting with eq. (9), which quite well fits the data. As can be seen, stress (at all levels of strain) can also double from the lower R to the higher R in the investigated microstructural anisotropy range. This supports the fact that the correct orientation of the microstructural anisotropy with respect to the load direction is a fundamental variable to optimize the energy absorption capacity of anisotropic polymer foams [63].

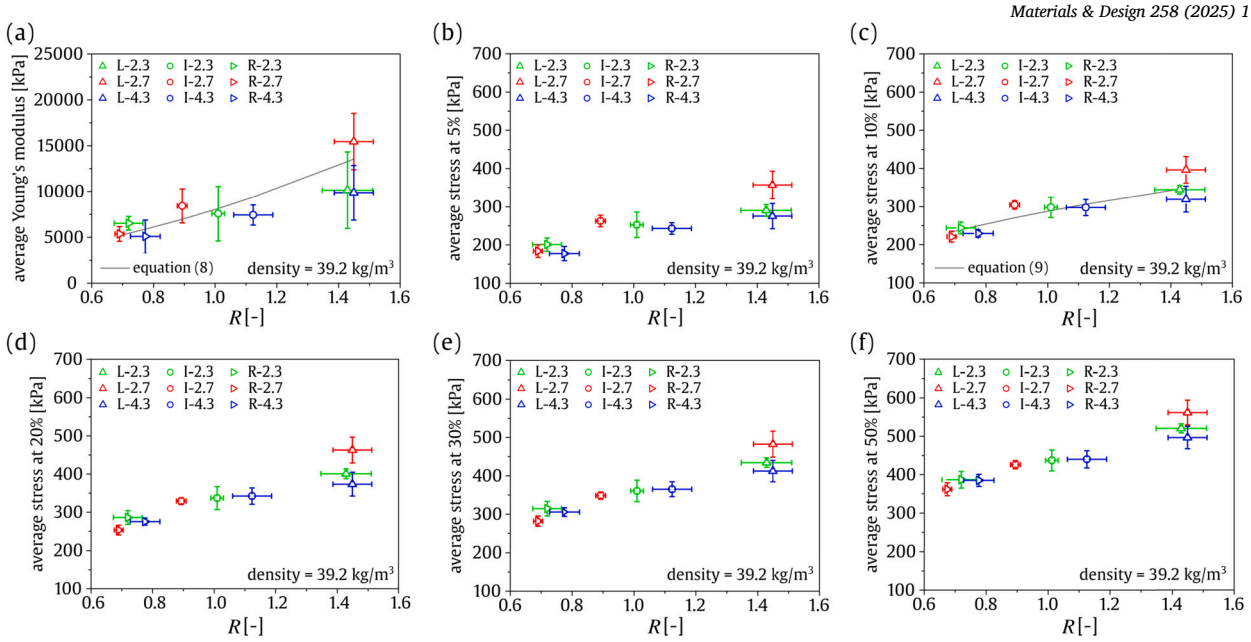

Fig. 7. Average moduli and average stresses versus R rescaled at density of 39.2 kg/m^3. (a) Young's moduli. (b), (c), (d), (e), (f) average stresses at 5%, 10%, 20%, 30%, 50% of strain, respectively.

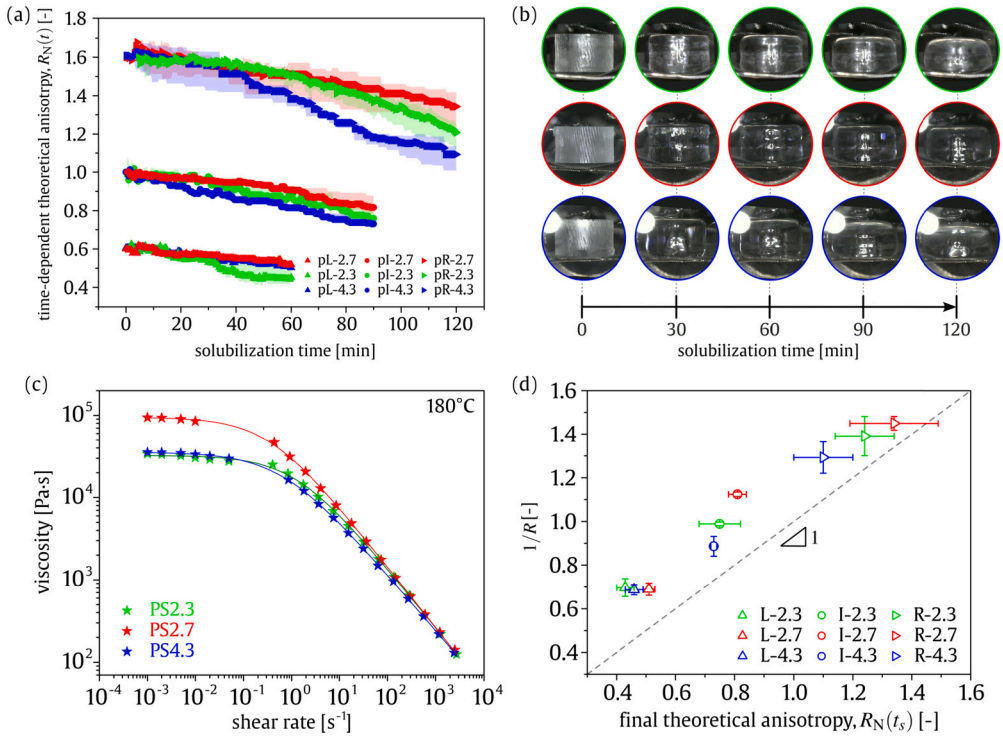

Fig. 8. Results of the sagging experiments. (a) Time-dependent theoretical anisotropy as a function of time with the estimated error bands (shadowed) for all the types of preforms and PSs. (b) Frames at different instants for preforms of type R. (c) Viscosity versus shear rate for the different PSs, where the lines are the best-fit with the Cross model (eq. (16)). (d) Microstructural anisotropy R of the PS foams versus the final theoretical anisotropy, $R_N(t_s)$, which corresponds to the anisotropy of the preform the instant before the pressure release (i.e., before the expansion and foam production). The dashed line corresponds to $R^{-1} = R_N(t_s)$.

Still, across the investigated range of R, foams produced from PS 4.3 consistently exhibit the lowest mechanical properties, and foams made from PS 2.3 generally perform worse than those from PS 2.7. This suggests that, when density and microstructural anisotropy are held constant, factors beyond M_n and M_w of the base PS influence the mechanical behavior of the foams [89].

6.4. Preforms sagging

To explain the differences in the values of R in the foams produced starting from the same preform but different polydispersity, we report the results of the sagging experiments in Fig. 8(a)-(d).

Fig. 8(a) reports the time-dependent theoretical anisotropy $R_N(t)$ versus the time. As expected, type L preforms have (i) less time to sag

Table 4
Best-fit of the Cross parameters of the viscosity versus shear rate curves of PS2.3, PS2.7 and PS4.3.

parameter	PS2.3	PS2.7	PS4.3
η_0 [Pa·s]	35400 ± 200	94700 ± 1500	32500 ± 600
λ [s]	1.5 ± 0.03	2.9 ± 0.1	0.075 ± 0.05
n [-]	0.682 ± 0.002	0.737 ± 0.004	0.723 ± 0.007

(since $t_s = 60$ min) and (ii) a minor characteristic shear stress acting on the preform itself, which scales with $\sim h^2/d$ [90]. Moving to preforms of type I and especially of type R, both quantities increase and the sagging effect becomes more and more pronounced. In particular, for preforms of type R, the sagging effect sensibly modifies the initial aspect ratio, which in the case of pR-4.3 almost tends to the aspect ratio pI-4.3. In such a case, the mechanical properties of the resulting foams from the pR-4.3 and pI-4.3 preforms will be closer: more precisely, the difference between the properties will be smaller compared to the difference expected from the mechanical properties of the foams obtained expanding the preforms pR-2.7 and pI-2.7 (as confirmed by Fig. 6(d)-(i)). In fact, from the three types of preform, it can also be seen that PS 2.7 is less prone to sag, while PS 4.3 seems to be more sensitive to the sagging effect.

In Fig. 8(b), we report the same frames of the sagging experiments of type R preforms of the three types of PS for a proper comparison. It can be clearly seen that at the end of the saturation time (i.e. 120 min), the pR-2.7 preform has not drastically changed its initial aspect ratio, while this is not true for pR-2.3 and especially for pR-4.3.

When considering the same type of preform, namely L, I, or R, the reason for the different sagging between different PSs can be found in their different values of zero-shear viscosity, η_0, during the solubilization step. During such a step and taking into account our processing conditions, we can estimate a weight fraction of CO_2 in all the PSs of $\sim 7\%$ [80], with a consequent strong decrease in the glass transition temperature up to (as a thumb rule) 8 °C per percentage point of solubilized CO_2 [76]. Hence, to properly characterize the viscosity of the different PSs in our processing conditions, we should perform the viscosity measurement at ~ 170 °C. For experimental limitations, we performed the measurement at 180 °C in the way described in subsection 5.4.

In Fig. 8(c), we report the viscosity versus the shear rate for the three PS at 180 °C. To find η_0, we fit the curves of Fig. 8(c) using the Cross equation, which reads:

$$\eta(\dot{\gamma}) = \frac{\eta_0}{1 + (\lambda\dot{\gamma})^n} \ , \tag{16}$$

where λ is an average time required for the chains to relax and n is a parameter related to the power law exponent in the shear thinning region. The best-fit values of the parameters of eq. (16) for the three PSs investigated are reported in Table 4.

As can be seen, the zero shear viscosity of PS 2.7 is roughly three times higher than the viscosity of PS 2.3 and PS 4.3, which is in fact in agreement with the sagging of the respective preforms reported in Fig. 8(a).

For further confirmation of the sagging of the preforms and its effect on the resulting foam morphology, we can consider the comparison between the values of the reciprocal of the microstructural anisotropy measured by SEM, $1/R$, and the values of the *final theoretical anisotropy*, i.e., the value of $R_N(t)$ at the time of expansion, $R_N(t_s)$. This comparison is reported in Fig. 8(d). As can be seen, the data align well on a straight line that is parallel to equation $R^{-1} = R_N(t_s)$, but shifted in the direction of cells more elongated/oriented in the radial direction (i.e. lower R). This effect may be due to microstructural relaxation before cooling guided by gravity.

6.5. Supporting the results: lower-density samples

In the present subsection, we produce and characterize isotropic lower-density foams (LD) of the three PSs to verify the reproducibility of the results and support the conclusions.

To produce such foams, we produce preforms with $R_{N_0} = 1.15$ but with a mass of 113 ± 1 mg, so that due to sagging it reaches $R_N(t_s) = 1$ and once expanded in the same mold as before, a lower density is achieved with respect to the previous samples. To verify that the reason for the different values of microstructural anisotropy is mainly the sagging of the preform, based on the results of Fig. 8 we adapt the solubilization time of the different PS preforms as follows: $t_s = 90$ min for the preform PS 2.3, $t_s = 105$ min for the preform PS 2.7, and $t_s = 75$ min for the preform 4.3. We underline that in all three cases, the solubilization time is enough to fully saturate the preform and hence to obtain a uniform foam, since such preforms are smaller than the previous ones, with a geometry comparable to that of the previous preform I. After production, we obtain $\rho = 31.3 \pm 0.4$ kg/m^3 for LD PS 2.3 foams, $\rho = 31.8 \pm 0.4$ kg/m^3 for LD PS 2.7 foams and $\rho = 30.9 \pm 0.8$ kg/m^3 for LD PS 4.3 foams. The results are shown in Fig. 9(a)-(f).

In Fig. 9(a)-(c) we report the SEM images of the LD foams with different polydispersity, which, as expected, are indeed very similar to the isotropic foams of Fig. 4(d)-(f). As can be clearly shown from Fig. 9(d), the trend in MCS of such LD foams confirms the trend obtained for the higher density foams (in transparency, from Fig. 5): this supports the conclusion that the difference in MCS is due to differences in the MWD of the base polymer, and more specifically, the presence of a low molecular weight tail. In Fig. 9(e), we compared the mechanical behavior of LD foams with the previous I foams: as expected [64], the stress-strain curves for LD foams are lower. However, such curves are comparable with those of higher density foams with a microstructural anisotropy of the order of 1.4: this supports the fact that by only changing the microstructural anisotropy, one can obtain the effect of a weight variation bigger than 20%, thus underlining the importance of a correct design of microstructural anisotropy. In Fig. 9(f), we report the reciprocal of microstructural anisotropy, $1/R$, as a function of $R_N(t_s)$ for LD samples, compared to the data of Fig. 8(d). In this case, the final theoretical anisotropy of the LD sample is only estimated based on the results of Fig. 8(a): we assume a change in the nominal theoretical anisotropy ratio equal to the one experienced by the preform pI-PS 2.3. This sagging is overestimated, because the shear stress acting on the LD preform causes a lower sagging [90]. We find that the values of $1/R$ for LD foams align nicely with the previous ones and show a smaller variation of the values of $1/R$ with respect to the values of higher-density I and R foams, correctly pointing in the direction of a reduction in sagging.

6.6. Design maps

In Fig. 10(a) and (b), we now propose examples of design maps for the Young's modulus and the stress @10% of the strain of transversely isotropic foams (in the direction of anisotropy), which can provide useful guidelines for engineers. The design maps are reported in the design space $\phi \in [0.01, 0.1]$ and $R \in [0.1, 3]$. It is worth noting that far from the investigated experimental range, the assumptions of the model may no longer be valid (e.g., changes in micro-mechanical mechanisms). The design curves (black lines) show correspond to the level curves of the function $\hat{E}/E_s$ for Fig. 10(a), and to the level curves of the function $\hat{\sigma}_{10\%}/\sigma_{ys}$ for Fig. 10(b). The experimental data are also reported for proper comparison. Using design maps, one can quantify the reduction in mass achieved by increasing the microstructural anisotropy (i.e., increasing R) of a transversely isotropic foam while maintaining its mechanical properties constant. Such design maps must be used with caution: it is important to note that they are obtained at a given γ value (herein, we used the obtained $\hat{\gamma}_E = 0.963$ and $\hat{\gamma}_\sigma = 0.778$), which must be the same γ shown by all the foams. Hence, discrepancies of the ex-

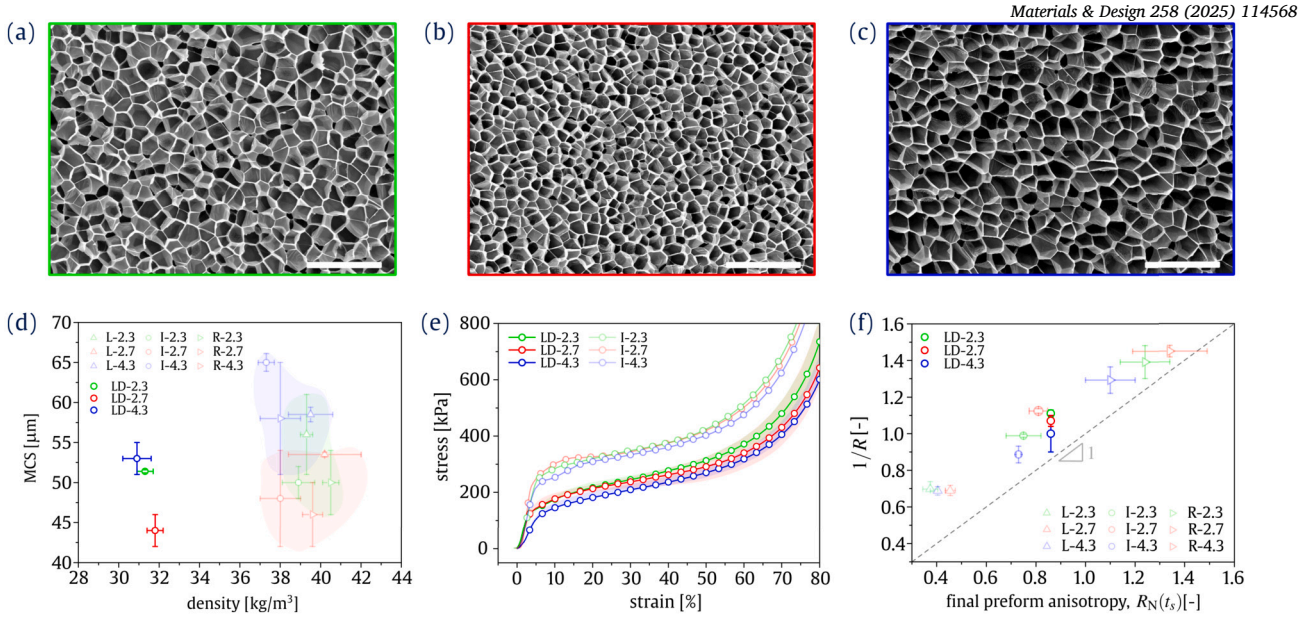

Fig. 9. Results of LD foams. (a), (b), (c) Are the SEM images of the foams I-LD-2.3, I-LD-2.7, I-LD-4.3, respectively, where the scale (white segment) is set to 200 μm. (d) Reports the MCS as a function of the density, where in transparency the results from Fig. 5 are reported. (e) Shows the stress-strain curves of the LD samples compared to the same types with higher density (which are in transparency). (f) Shows R versus $R_N(t_s)$ (estimated) for LD foams, compared in transparency to the results of Fig. 8(d).

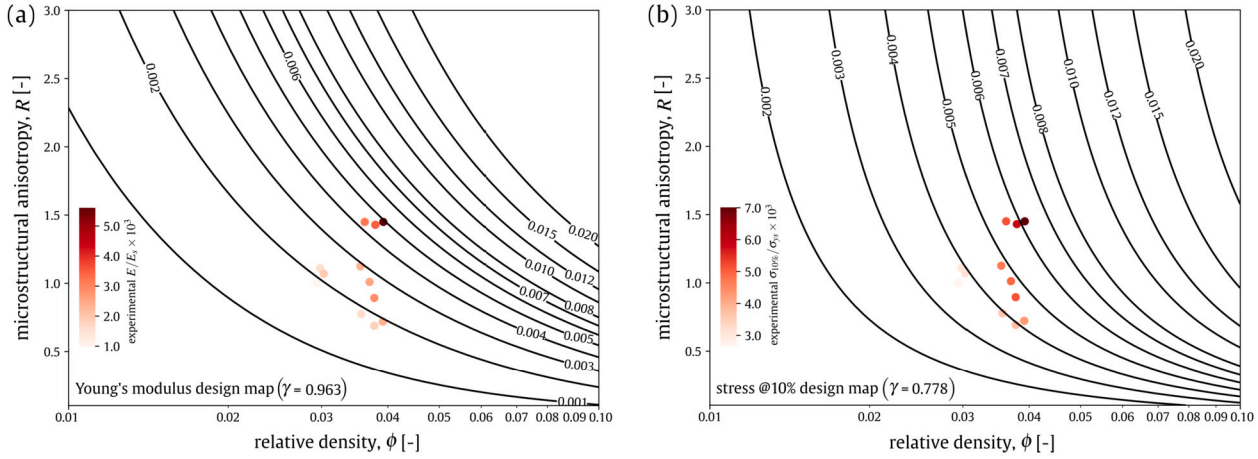

Fig. 10. Example of design maps, with experimental data reported for comparison and design curves are in black. (a) Design map for the Young's modulus. (b) Design map for the stress @10% of strain.

perimental values from the values of the design curves can be ascribed to a given distance from the γ by which maps are obtained.

In addition, such design maps are, in principle, generalizable to any base polymer. However, in the case of semicrystalline polymers, the induced anisotropy may also lead to anisotropic crystallization within the cell walls, potentially influencing the mechanical properties of the matrix and, consequently, those of the foam. Accounting for this effect would require the introduction of an additional parameter into the model, which would alter the curves in the design maps.

7. Conclusions

Even if polymer foams are ubiquitous in everyday life, many questions remain about the relationship between their microstructure and the related macroscopic mechanical behavior. In their mechanics, many (in principle, independent) parameters play a role, such as base polymer properties, density, and microstructural anisotropy. In the present research, we have focused our attention on the effect of microstructural anisotropy on the quasi-static uniaxial mechanics of anisotropic polymer foams. We have produced transversely anisotropic PS foams in the (average) density range $37.3 - 41.2$ kg/m^3 by expanding well-designed preforms through physical batch foaming, and we have characterized their uniaxial compression mechanics and microstructure. We have found that, while maintaining a constant density, the sole microstructural anisotropy in the experimentally investigated range can increase/decrease their linear and nonlinear mechanical properties up to more than three times. This increase/decrease can be reasonably described by the rectangular homogenized closed-cell model proposed by Gibson and Ashby [64], where the aspect ratio of the cell is substituted with a homogenized aspect ratio of the microstructure - the microstructural anisotropy - which can be obtained according to ASTM D 3756-15 [84]. We find that all mechanical properties follow a consistent trend with respect to R (described by eq. (8) or eq. (9)), which, however, seems vertically shifted depending on the base PS. This shift may arise from variations in frozen stresses within the cell walls, differences in the bulk material properties, cell diameter, and variations in the thickness of the struts and walls. However, this aspect requires further investigation. We found that the MWD of the base PS affects how much the

preform sags, which impacts the final foam microstructure. In fact, the zero-shear viscosity, which controls sagging, depends on the MWD. We supported our findings with an additional experimental campaign on lower density foams, which is consistent with all previous results. In conclusion, we also propose design maps for the Young's modulus and the stress at 10% of strain for transversely isotropic foams: from such maps, the density and the microstructural anisotropy can be calibrated to target specific mechanical properties. We believe that these results can offer significant understanding of the relationship between process, microstructure, and properties in anisotropic polymer foams, promoting a more effective and efficient approach to designing these materials.

CRediT authorship contribution statement

Paolo Iaccarino: Writing – review & editing, Writing – original draft, Visualization, Validation, Software, Methodology, Investigation, Formal analysis, Data curation, Conceptualization. **Pietro Sisti:** Writing – original draft, Validation, Investigation, Formal analysis, Data curation. **Dino Ferri:** Writing – review & editing, Writing – original draft, Validation, Supervision, Methodology, Investigation, Formal analysis, Data curation, Conceptualization. **Ernesto Di Maio:** Writing – review & editing, Writing – original draft, Visualization, Validation, Supervision, Resources, Project administration, Methodology, Conceptualization.

Declaration of competing interest

The authors declare that they have no known competing financial interests or personal relationships that could have appeared to influence the work reported in this paper.

Acknowledgements

The authors would like to thank Irene Polloni, Massimo Vighi, Paolo Corradini, and Claudio Mancinelli (Versalis S.p.A, Mantova, Italy) for their constant support in data collection and analysis; Leonardo Castellani (Versalis S.p.A, Mantova, Italy, currently retired) for the fruitful discussions regarding the fracture of polymer and of polymer foams; Pasquale Strazzullo (University of Naples Federico II, Naples, Italy) for his help in developing CAD models for the visualization of the experimental equipment and the preforms expansion.

Appendix A

A.1. Error on the density measurement

Given eq. (3), the absolute error on the measured density of the foams, $|\delta_\rho|$, can be computed according to the linear error propagation theory (hence obtaining an overestimated value) as follows:

$$|\delta_\rho| = \rho\left(\frac{|\delta_{m_a}|}{|m_a|} + \frac{|\delta_{m_a}| + |\delta_{m_w}|}{|m_a - m_w|} + \frac{|\delta_{\rho_w}| + |\delta_{\rho_a}|}{|\rho_w - \rho_a|}\right) + |\delta_{\rho_a}| \ , \tag{A.1}$$

where δ_{m_a}, δ_{m_w}, δ_{ρ_w} and δ_{ρ_a} are the absolute errors of m_a, m_w, ρ_w and ρ_a, respectively.

A.2. Uncertainty determination of R

The uncertainty in determining R, e_R can be obtained by propagating the standard error of the mean of the two chord distributions:

$$\mathrm{e}_R = R\sqrt{\left(\frac{\mathrm{SD}_{C_r}}{C_r\sqrt{N_r}}\right)^2 + \left(\frac{\mathrm{SD}_{C_l}}{C_l\sqrt{N_l}}\right)^2} \ , \tag{A.2}$$

where SD_{C_r} and SD_{C_l} are the standard deviations of the distributions of the radial and longitudinal chords, respectively, while N_r and N_l are the number of chords obtained by the ILM in the radial and longitudinal directions, respectively.

The uncertainty on the average between the values R of the two samples per type is assumed as $\delta_R = \max\left(\delta_{\text{half-spread}_R}, \mathrm{pe}_R\right)$, that is, the maximum value between the half-spread $\delta_{\text{half-spread}_R} = |R_1 - R_2|/2$ and the propagation error $\mathrm{pe}_R = (1/2)\sqrt{\mathrm{e}_{R_1}^2 + \mathrm{e}_{R_2}^2}$.

A.3. Derivation of the expression of MCS and its uncertainty

In this subsection we generalize for the anisotropic cases the derivation of cell size and shape using the ILM reported in [84] for the isotropic case. We assume that the cell shape is spheroidal (prolate or oblate spheroids) and that all cells are oriented along the longitudinal direction. With these assumptions, the cells have circular symmetry in the radial plane (for both prolate and oblate spheroid cases). We name the average spheroid semiaxes as $\mathrm{A_l}$ in the longitudinal direction and $\mathrm{A_r}$ in the radial direction. In subsection 5.2 the procedure for determining the average measured chord length in the longitudinal direction $\mathrm{C_l}$ and in the radial direction $\mathrm{C_r}$ of the randomly truncated cells is described, and the relationship between Cr ($\mathrm{C_l}$) and Ar ($\mathrm{A_l}$) can be obtained as described below.

With our assumptions, when cells are randomly truncated by a longitudinal plane as described in subsection 5.2, ellipses appear on the cut surface. We name $\mathrm{a_l}$ and $\mathrm{a_r}$ the average ellipse semiaxes in the longitudinal and radial directions on the cut surface, respectively. Therefore, the ellipse equation is

$$\frac{\mathrm{x}^2}{\mathrm{a_r}^2} + \frac{\mathrm{y}^2}{\mathrm{a_l}^2} = 1 \ , \tag{A.3}$$

and the relationship between Cr ($\mathrm{C_l}$) and $\mathrm{a_r}$ ($\mathrm{a_l}$) can be calculated as follows:

$$\frac{\mathrm{C_l}}{2} = \hat{\mathrm{y}} \overset{\text{def.}}{=} \frac{\int_0^{\mathrm{a_r}} \mathrm{y(x)dx}}{\int_0^{\mathrm{a_r}} \mathrm{dx}} = \mathrm{a_l}\frac{\pi}{4} \quad \frac{\mathrm{C_r}}{2} = \hat{\mathrm{x}} \overset{\text{def.}}{=} \frac{\int_0^{\mathrm{a_l}} \mathrm{x(y)dy}}{\int_0^{\mathrm{a_l}} \mathrm{dy}} = \mathrm{a_r}\frac{\pi}{4}, \ . \tag{A.4}$$

The relationship between $\mathrm{a_l}$ ($\mathrm{a_r}$) and $\mathrm{A_l}$ ($\mathrm{A_r}$) can be obtained with analogous calculus:

$$\mathrm{a_l} = \mathrm{A_l}\frac{\pi}{4}, \quad \mathrm{a_r} = \mathrm{A_r}\frac{\pi}{4} \ . \tag{A.5}$$

Combining eq. (A.4) and eq. (A.5) yields the following:

$$\mathrm{A_l} = \frac{\mathrm{C_l}}{2}\left(\frac{4}{\pi}\right)^2, \ \mathrm{A_r} = \frac{\mathrm{C_r}}{2}\left(\frac{4}{\pi}\right)^2 \ . \tag{A.6}$$

The uncertainty of MCS, δ_{MCS}, can be obtained as follows:

$$\delta_{\mathrm{MCS}} = \left(\frac{4}{\pi}\right)^2 \frac{\sqrt{N_l\sigma_{C_l}^2 + N_r\sigma_{C_r}^2}}{N_l + N_r} \ . \tag{A.7}$$

A.4. Density-rescaling coefficients and fitting parameters

In Table A.1, we report the density-rescaling coefficients for Young's moduli and the stresses (c^E and c^σ, respectively) for each type of foam. The adopted rescaling density is 39.2 kg/m^3 ($\phi^* = 0.0373$). The density-rescaling coefficients refer to the following fitting values: $\hat{\gamma}_E = 0.963 \pm 0.004$; $\hat{\gamma}_\sigma = 0.778 \pm 0.007$.

Appendix B. Supplementary material

Supplementary material related to this article can be found online at https://doi.org/10.1016/j.matdes.2025.114568.

Data availability

Data will be made available on request.

Table A.1
Density-rescaling coefficients for each type of foam. The target density is 39.2 kg/m^3.

coefficient	L-2.3	I-2.3	R-2.3	L-2.7	I-2.7	R-2.7	L-4.3	I-4.3	R-4.3
c^E [-]	0.975	1.02	0.939	0.920	0.986	0.987	1.053	1.079	1.066
c^σ [-]	0.982	1.012	0.948	0.943	0.988	0.989	1.037	1.063	1.055

References

[1] M. Tomin, Á. Kmetty, Polymer foams as advanced energy absorbing materials for sports applications—a review, J. Appl. Polym. Sci. 139 (2022) 51714.
[2] N. Obaid, M.T. Kortschot, M. Sain, Lightweight thermoset foams in automotive applications, in: Lightweight and Sustainable Materials for Automotive Applications, CRC Press, 2017, pp. 401–422.
[3] B. Furet, P. Poullain, S. Garnier, 3d printing for construction based on a complex wall of polymer-foam and concrete, Addit. Manuf. 28 (2019) 58–64.
[4] F. Lizalde-Arroyo, V. Bernardo, M.Á. Rodríguez-Pérez, J. Martín-de León, Exploring transparent ultra–nanocellular high-performance polymers: polyetherimide (pei), Mater. Des. (2025) 114222.
[5] X. Li, Y. Zong, W. Li, J. Qian, Z. Qiang, C. Ye, M. Zhu, Achieving ultrahigh transparency and superior mechanical properties in flexible polyimide nanofoams through co2 foaming for thermal insulation, Adv. Funct. Mater. 34 (2024) 2409498.
[6] Z. Wang, G. Wang, Z. Xu, J. Chai, G. Zhao, Innovative crosslinking and foaming strategies for advancing biodegradable composite foams: enhancing foamability, flexibility, and thermal insulation, Mater. Des. 253 (2025) 113895.
[7] K. Zhang, X. Zhang, Q. Gao, M. Chan, S. Zhang, J. Li, W.-H. Liao, Ultrahigh energy-dissipation and multifunctional auxetic polymeric foam inspired by balloon art, Composites, Part A, Appl. Sci. Manuf. 167 (2023) 107435.
[8] Q. Zhang, X. Yu, Y. Xia, D. Zhang, R.S. Lakes, K.W. Wojciechowski, F. Scarpa, The shear performance of uniaxially thermoformed auxetic polymer foams, Composites, Part B, Eng. 286 (2024) 111791.
[9] K. Chung, X. Feng, Y. Jiang, K. Li, J. Chen, Y. Han, L. Tan, Z. Du, Shape memory polyurethane foams with tunable mechanical properties and radiation tolerance for breast repair and reconstruction, J. Biomed. Mater. Res., Part A 113 (2025) e37821.
[10] X. Jia, W. Zhong, Y. Chen, D. Hu, J. Sun, Y. Peng, J. Yu, X. Jiang, L. Zhao, Density gradient structure foams prepared by novel two-step foaming strategy: performance, simulation and optimization, Composites, Part B, Eng. 288 (2025) 111890.
[11] P. Iaccarino, E. Maresca, S. Morganti, F. Auricchio, E. Di Maio, Topologically optimized graded foams, Adv. Eng. Mater. 26 (2024) 2301798.
[12] L. Meng, H. Liu, L. Yu, S. Khalid, L. Chen, T. Jiang, Q. Li, Elastomeric foam prepared by supercritical carbon dioxide, J. Appl. Polym. Sci. 134 (2017).
[13] I.R. Henriques, L. Rouleau, D.A. Castello, L.A. Borges, J.-F. Deü, Viscoelastic behavior of polymeric foams: experiments and modeling, Mech. Mater. 148 (2020) 103506.
[14] S. Deschanel, L. Vanel, N. Godin, E. Maire, G. Vigier, S. Ciliberto, Mechanical response and fracture dynamics of polymeric foams, J. Phys. D, Appl. Phys. 42 (2009) 214001.
[15] S.M. Husainie, S.U. Khattak, J. Robinson, H.E. Naguib, A comparative study on the mechanical properties of different natural fiber reinforced free-rise polyurethane foam composites, Ind. Eng. Chem. Res. 59 (2020) 21745–21755.
[16] X. Liu, K. Yu, P. Chen, From polymer matrix to cell structure: Stg/tems/pu energy-absorbing foamed composites with strain rate-dependent and bimodal cellular structure, Mater. Des. 250 (2025) 113638.
[17] A.M. Harris, E.C. Lee, Improving mechanical performance of injection molded pla by controlling crystallinity, J. Appl. Polym. Sci. 107 (2008) 2246–2255.
[18] T. Parenteau, G. Ausias, Y. Grohens, P. Pilvin, Structure, mechanical properties and modelling of polypropylene for different degrees of crystallinity, Polymer 53 (2012) 5873–5884.
[19] S. Yao, D. Hu, Z. Xi, T. Liu, Z. Xu, L. Zhao, Effect of crystallization on tensile mechanical properties of pet foam: experiment and model prediction, Polym. Test. 90 (2020) 106649.
[20] M. Wu, F. Wu, Q. Ren, Z. Weng, H. Luo, L. Wang, W. Zheng, Effect of crystalline structure on the cell morphology and mechanical properties of polypropylene foams fabricated by core-back foam injection molding, J. Appl. Polym. Sci. 138 (2021) 51370.
[21] P. Li, B. Lan, Q. Zhang, Q. Yang, P. Gong, C.B. Park, G. Li, Microcellular foams simultaneous reinforcing and toughening strategy of combining nano-fibrillation network and supercritical solid-state foaming, Polymer 252 (2022) 124928.
[22] D. Rusakov, A. Menner, F. Spieckermann, H. Wilhelm, A. Bismarck, Morphology and properties of foamed high crystallinity peek prepared by high temperature thermally induced phase separation, J. Appl. Polym. Sci. 139 (2022) 51423.
[23] J.-B. Bao, T. Liu, L. Zhao, G.-H. Hu, X. Miao, X. Li, Oriented foaming of polystyrene with supercritical carbon dioxide for toughening, Polymer 53 (2012) 5982–5993.
[24] B. Obi, Polymeric Foams Structure-Property-Performance: A Design Guide, William Andrew, 2017.
[25] B. Koohbor, N. Pagliocca, G. Youssef, A multiscale experimental approach to characterize micro-to-macro transition length scale in polymer foams, Mech. Mater. 161 (2021) 104006.
[26] V. Srivastava, R. Srivastava, On the polymeric foams: modeling and properties, J. Mater. Sci. 49 (2014) 2681–2692.
[27] D. Walicki, P. Zawistowski, J. Ryszkowska, Exploring the microstructure–property relationship in polymer foams using advanced statistical methods, machine learning and deep learning: a review, Comput. Mater. Sci. 256 (2025) 113909.
[28] M.F. Ashby, R.M. Medalist, The Mechanical Properties of Cellular Solids, 1983.
[29] F. Ramsteiner, N. Fell, S. Forster, Testing the deformation behaviour of polymer foams, Polym. Test. 20 (2001) 661–670.
[30] F. Saint-Michel, L. Chazeau, J.-Y. Cavaillé, E. Chabert, Mechanical properties of high density polyurethane foams: I. effect of the density, Compos. Sci. Technol. 66 (2006) 2700–2708.
[31] E. Linul, L. Marsavina, T. Voiconi, T. Sadowski, Study of factors influencing the mechanical properties of polyurethane foams under dynamic compression, J. Phys. Conf. Ser. 451 (2013) 012002.
[32] A.D. Drozdov, J. de Claville Christiansen, The effect of porosity on elastic moduli of polymer foams, J. Appl. Polym. Sci. 137 (2020) 48449.
[33] S. De Carolis, C. Putignano, L. Soria, G. Carbone, Effect of porosity and pore size distribution on elastic modulus of foams, Int. J. Mech. Sci. 261 (2024) 108661.
[34] M. Saha, H. Mahfuz, U. Chakravarty, M. Uddin, M.E. Kabir, S. Jeelani, Effect of density, microstructure, and strain rate on compression behavior of polymeric foams, Mater. Sci. Eng. A 406 (2005) 328–336.
[35] D. Zenkert, M. Burman, Tension, compression and shear fatigue of a closed cell polymer foam, Compos. Sci. Technol. 69 (2009) 785–792.
[36] N. Mills, H. Zhu, The high strain compression of closed-cell polymer foams, J. Mech. Phys. Solids 47 (1999) 669–695.
[37] S. Gaitanaros, S. Kyriakides, On the effect of relative density on the crushing and energy absorption of open-cell foams under impact, Int. J. Impact Eng. 82 (2015) 3–13.
[38] K.B. Bhagavathula, C.S. Meredith, S. Ouellet, S.S. Satapathy, D.L. Romanyk, J.D. Hogan, Density, microstructure, and strain-rate effects on the compressive response of polyurethane foams, Exp. Mech. (2022) 1–15.
[39] J. Chen, L. Cheng, D. Hu, Y. Si, J. Jiang, Effect of chemical foaming process parameters on the performance of epoxy foam and parameter optimization strategies, Adv. Eng. Mater. 27 (2025) 2402115.
[40] L. Marşavina, E. Linul, Fracture toughness of rigid polymeric foams: a review, Fatigue Fract. Eng. Mater. Struct. 43 (2020) 2483–2514.
[41] M.C. Hawkins, B. O'Toole, D. Jackovich, Cell morphology and mechanical properties of rigid polyurethane foam, J. Cell. Plast. 41 (2005) 267–285.
[42] J.E. Weller, V. Kumar, Solid-state microcellular polycarbonate foams. II. The effect of cell size on tensile properties, Polym. Eng. Sci. 50 (2010) 2170–2175.
[43] R. Brezny, D.J. Green, The effect of cell size on the mechanical behavior of cellular materials, Acta Metall. Mater. 38 (1990) 2517–2526.
[44] E. Sadek, N. Fouad, Finite element modeling of compression behavior of extruded polystyrene foam using x-ray tomography, J. Cell. Plast. 49 (2013) 161–191.
[45] Y. Chen, R. Das, M. Battley, Effects of cell size and cell wall thickness variations on the stiffness of closed-cell foams, Int. J. Solids Struct. 52 (2015) 150–164.
[46] P. Zhu, J. Rong, S. Wang, Z. Chen, Experimental and analytical study on the compressive behavior of pmi foam with different densities and cell sizes under intermediate strain rates, Polym. Test. 140 (2024) 108593.
[47] M. Vesenjak, L. Krstulović-Opara, Z. Ren, Ž. Domazet, Cell shape effect evaluation of polyamide cellular structures, Polym. Test. 29 (2010) 991–994.
[48] L. Xie, K.C. Chan, The effect of strut geometry on the yielding behaviour of open-cell foams, Int. J. Mech. Sci. 48 (2006) 249–255.
[49] K. Li, X.-L. Gao, G. Subhash, Effects of cell shape and strut cross-sectional area variations on the elastic properties of three-dimensional open-cell foams, J. Mech. Phys. Solids 54 (2006) 783–806.
[50] A. Huber, L. Gibson, Anisotropy of foams, J. Mater. Sci. 23 (1988) 3031–3040.
[51] S. Fushimi, T. Nagakura, A. Yonezu, Experimental and numerical investigations of the anisotropic deformation behavior of low-density polymeric foams, Polym. Test. 63 (2017) 605–613.
[52] F. Rahimidehgolan, W. Altenhof, Compressive behavior and deformation mechanisms of rigid polymeric foams: a review, Composites, Part B, Eng. 253 (2023) 110513.
[53] M. Marvi-Mashhadi, C. Lopes, J. LLorca, Modelling of the mechanical behavior of polyurethane foams by means of micromechanical characterization and computational homogenization, Int. J. Solids Struct. 146 (2018) 154–166.
[54] M. Rejab, M. Sani, M. Noor, K. Kadirgama, M. Rahman, A. Alias, Mechanical behaviour of polymeric foam core at various orientation angles, WIT Trans. Built Environ. 112 (2010) 429–438.
[55] V. Tita, M.F. Caliri, R.A. Angélico, R.B. Canto, Experimental analyses of the poly (vinyl chloride) foams' mechanical anisotropic behavior, Polym. Eng. Sci. 52 (2012) 2654–2663.
[56] F. Rahimidehgolan, Y. Liu, W. Altenhof, Experimental, numerical and analytical investigations on the elevated strain rate compressive behavior of high-performance pes foam up to 200 s- 1, Int. J. Impact Eng. 161 (2022) 104088.

[57] Y. Tang, W. Zhang, X. Jiang, J. Zhao, W. Xie, T. Chen, Experimental investigations on phenomenological constitutive model of closed-cell pvc foam considering the effects of density, strain rate and anisotropy, Composites, Part B, Eng. 238 (2022) 109885.
[58] Z. Tu, V. Shim, C. Lim, Plastic deformation modes in rigid polyurethane foam under static loading, Int. J. Solids Struct. 38 (2001) 9267–9279.
[59] M. Maurer, B.-H. Choi, K. Sehanobish, G. Vogel, Modeling the compressive fracture behavior of foams for energy absorption, J. Cell. Plast. 47 (2011) 373–393.
[60] P. Li, Y.B. Guo, M.W. Zhou, V.P. Shim, Response of anisotropic polyurethane foam to compression at different loading angles and strain rates, Int. J. Impact Eng. 127 (2019) 154–168.
[61] M. Marvi-Mashhadi, C. Lopes, J. LLorca, Effect of anisotropy on the mechanical properties of polyurethane foams: an experimental and numerical study, Mech. Mater. 124 (2018) 143–154.
[62] Y. Liu, F. Rahimidehgolan, W. Altenhof, Anisotropic compressive behavior of rigid pvc foam at strain rates up to 200 s- 1, Polym. Test. 91 (2020) 106836.
[63] Y. Mosleh, K. Vanden Bosche, B. Depreitere, J. Vander Sloten, I. Verpoest, J. Ivens, Effect of polymer foam anisotropy on energy absorption during combined shear-compression loading, J. Cell. Plast. 54 (2018) 597–613.
[64] L. Gibson, M. Ashby, Cellular Solids, Structure and Properties, second edition, Cambridge University Press, 1997.
[65] C. Calladine, R. English, Strain-rate and inertia effects in the collapse of two types of energy-absorbing structure, Int. J. Mech. Sci. 26 (1984) 689–701.
[66] S. Luan, A.M. Kraynik, S. Gaitanaros, Microscopic and macroscopic instabilities in elastomeric foams, Mech. Mater. 164 (2022) 104124.
[67] S. Wang, Y. Zhu, J. Yu, L. Wang, Z. Zheng, Anisotropic mechanics of cell-elongated structures: finite element study based on a 3d cellular model, Thin-Walled Struct. 205 (2024) 112405.
[68] V. Bernardo, E. Laguna-Gutierrez, A. Lopez-Gil, M.A. Rodriguez-Perez, Highly anisotropic crosslinked hdpe foams with a controlled anisotropy ratio: production and characterization of the cellular structure and mechanical properties, Mater. Des. 114 (2017) 83–91.
[69] T. Sauter, K. Kratz, S. Madbouly, F. Klein, M. Heuchel, A. Lendlein, Anisotropy effects in the shape-memory performance of polymer foams, Macromol. Mater. Eng. 306 (2021) 2000730.
[70] L. Oliveira-Salmazo, A. Lopez-Gil, F. Silva-Bellucci, A.E. Job, M.A. Rodriguez-Perez, Natural rubber foams with anisotropic cellular structures: mechanical properties and modeling, Ind. Crop. Prod. 80 (2016) 26–35.
[71] ASTM Committee D-11 on Rubber, Standard Test Method for Assignment of the DSC Procedure for Determining Tg of a Polymer or an Elastomeric Compound, ASTM International, 2008.
[72] C. Marrazzo, E. Di Maio, S. Iannace, L. Nicolais, Process-structure relationships in pcl foaming, J. Cell. Plast. 44 (2008) 37–52.
[73] L. Miele, E. Di Lorenzo, C. Guissart, E. Di Maio, Liquid foaming of tpu with methylal, Heliyon 10 (2024).
[74] Y. Sato, T. Takikawa, S. Takishima, H. Masuoka, Solubilities and diffusion coefficients of carbon dioxide in poly (vinyl acetate) and polystyrene, J. Supercrit. Fluids 19 (2001) 187–198.
[75] M. Perez-Blanco, J.R. Hammons, R.P. Danner, Measurement of the solubility and diffusivity of blowing agents in polystyrene, J. Appl. Polym. Sci. 116 (2010) 2359–2365.
[76] R. Gendron, M.F. Champagne, Y. Delaviz, M.E. Polasky, Foaming polystyrene with a mixture of co2 and ethanol, J. Cell. Plast. 42 (2006) 127–138.
[77] E. Kiran, J.C. Hassler, High-pressure torsional braid analysis (hp-tba): a new technique for assessment of thermal transitions and changes in moduli of polymers exposed to supercritical or compressed fluids, J. Supercrit. Fluids 143 (2019) 223–231.
[78] J.A. Sarver, J.C. Hassler, E. Kiran, Linking thermophysical and rheological properties to the selection of co2 foaming conditions of rubbery elastomers using the relative rigidity reduction path, J. Supercrit. Fluids 166 (2020) 105015.
[79] J.A. Sarver, G.A. van Horn, E. Kiran, Glass transition behavior of poly (methyl methacrylate) in compressed carbon dioxide revisited–new perspectives, Thermochim. Acta 713 (2022) 179250.
[80] M.J. Wingert, S. Shukla, K.W. Koelling, D.L. Tomasko, L.J. Lee, Shear viscosity of co2-plasticized polystyrene under high static pressures, Ind. Eng. Chem. Res. 48 (2009) 5460–5471.
[81] D. Tammaro, V. Contaldi, M.P. Carbone, E. Di Maio, S. Iannace, A novel lab-scale batch foaming equipment: the mini-batch, J. Cell. Plast. 52 (2016) 533–543.
[82] J. Schindelin, I. Arganda-Carreras, E. Frise, V. Kaynig, M. Longair, T. Pietzsch, S. Preibisch, C. Rueden, S. Saalfeld, B. Schmid, et al., Fiji: an open-source platform for biological-image analysis, Nat. Methods 9 (2012) 676–682.
[83] R. Weast, Handbook of Chemistry and Physics, 53rd edition, Chemical Rubber Pub., 1972, https://books.google.it/books?id=aXHKtAEACAAJ.
[84] ASTM Committee D-20 on Plastics, Standard Test Method for Cell Size of Rigid Cellular Plastics, ASTM International, 2015.
[85] E. Reverchon, S. Cardea, Production of controlled polymeric foams by supercritical co2, J. Supercrit. Fluids 40 (2007) 144–152.
[86] C.M. Stafford, T.P. Russell, T.J. McCarthy, Expansion of polystyrene using supercritical carbon dioxide: effects of molecular weight, polydispersity, and low molecular weight components, Macromolecules 32 (1999) 7610–7616.
[87] J. Andersons, M. Kirpluks, L. Stiebra, U. Cabulis, Anisotropy of the stiffness and strength of rigid low-density closed-cell polyisocyanurate foams, Mater. Des. 92 (2016) 836–845.
[88] M.L. Crowder, A.A. Ogale, E.R. Moore, B.D. Dalke, Interrelationship of strength and flow characteristics of polystyrene, Polym. Eng. Sci. 34 (1994) 1497–1505.
[89] H.W. McCormick, F.M. Brower, L. Kin, The effect of molecular weight distribution on the physical properties of polystyrene, J. Polym. Sci. 39 (1959) 87–100.
[90] M.T. Hossain, R.H. Ewoldt, Protorheology, J. Rheol. 68 (2024) 113–144.